



**HAL**  
open science

## Defects and microstructure of highly conducting Al-doped ZnO ceramics obtained via spark plasma sintering

Haoxian Chen, Qianying Sun, Tian Tian, Liaoying Zheng, Maud Barré, Isabelle Monot-Laffez, Malgorzata Makowska-Janusik, Guorong Li, Abdel Hadi Kassiba

### ► To cite this version:

Haoxian Chen, Qianying Sun, Tian Tian, Liaoying Zheng, Maud Barré, et al.. Defects and microstructure of highly conducting Al-doped ZnO ceramics obtained via spark plasma sintering. *Journal of the European Ceramic Society*, 2020, 40 (15), pp.5529-5534. 10.1016/j.jeurceramsoc.2020.06.030 . hal-03219941

HAL Id: hal-03219941

<https://univ-tours.hal.science/hal-03219941>

Submitted on 22 Aug 2022

**HAL** is a multi-disciplinary open access archive for the deposit and dissemination of scientific research documents, whether they are published or not. The documents may come from teaching and research institutions in France or abroad, or from public or private research centers.

L'archive ouverte pluridisciplinaire **HAL**, est destinée au dépôt et à la diffusion de documents scientifiques de niveau recherche, publiés ou non, émanant des établissements d'enseignement et de recherche français ou étrangers, des laboratoires publics ou privés.



Distributed under a Creative Commons Attribution - NonCommercial 4.0 International License

**Defects and microstructure of highly conducting Al-doped ZnO ceramics  
obtained via spark plasma sintering**

**Haoxian Chen<sup>a,b,1</sup>, Qianying Sun<sup>a,b,c,1</sup>, Tian Tian<sup>a,b</sup>, Liaoying Zheng<sup>a,b</sup>, Maud Barré<sup>c</sup>, Isabelle Monot-Laffez<sup>d</sup>, Małgorzata Makowska-Janusik<sup>e</sup>, Guorong Li<sup>a,b,\*</sup>, Abdel Hadi Kassiba<sup>c,\*</sup>**

<sup>a</sup> Key Laboratory of Inorganic Functional Materials and Devices, Shanghai Institute of Ceramics, Chinese Academy of Sciences, 1295 Dingxi Road, Shanghai 200050, China

<sup>b</sup> Center of Materials Science and Optoelectronics Engineering, University of Chinese Academy of Sciences, Beijing 100049, China

<sup>c</sup> Institute of Molecules and Materials of Le Mans (IMMM) – UMR – CNRS 6283, Le Mans Université, 72085, Le Mans Cedex 9, France

<sup>d</sup> Laboratoire GREMAN UMR 7347, Université de Tours-CNRS-INSA-CVL, IUT de BLOIS, 15 rue de la chocolaterie, CS 32903, 41029 Blois Cedex, France

<sup>e</sup> Institute of Physics, Faculty of Mathematics and Natural Science, Jan Długosz University in Częstochowa, Al. Armii Krajowej 13/15, 42200 Częstochowa, Poland

**Abstract**

Al-doped ZnO ceramics were sintered by conventional sintering method and spark plasma sintering (SPS) respectively. Electrical properties and microstructure have been investigated by various measurements. **The samples sintered via SPS exhibit a huge electrical conductivity, up to  $3.0 \times 10^5$  S/m at room temperature, which was much higher than that of the sample sintered via the conventional sintering. Structural**

and morphological characterizations pointed out that the further incorporation of Al ions and the absence of secondary phase, contribute to the increase of the carrier concentration. Raman spectroscopy revealed the occurrence of structural distortions and a disorder induced by Al doping. Photoluminescence spectra were interpreted by different electronic active defects such as the defect complexes ( $\text{Al}_{\text{Zn}}\text{-Zn}_i$ ) which play a key for the high electrical conductivity. Thus, SPS and Al doping modified the microstructure and the concentration of the electronic active defects to ensure high electrical conductivities in doped ZnO-based ceramics.

**Keywords:** Al-doped; ZnO ceramic; SPS; high conductivity;  $\text{Al}_{\text{Zn}}\text{-Zn}_i$  complex

\*: corresponding authors G. Li (grli@mail.sic.ac.cn), A. Kassiba (Abdelhadi.Kassiba@univ-lemans.fr)

<sup>1</sup>: These authors contributed equally to this work.

## 1. Introduction

As a well-known II-VI semiconducting material, ZnO exhibits some unique properties such as wide band gap ( $E_g = 3.37$  eV), large exciton binding energy (60 meV) and high electrical conductivity induced by suitable doping. These features justify that ZnO-based devices have been widely used in regions of varistors, gas sensors, transparent electrodes, UV-light emitting diodes, piezoelectric and thermoelectric devices [1-3]. In addition, intrinsic defects in ZnO lead to n-type semiconducting behavior which may be modulated by doping, and this feature has

also drawn extensive attention from **the fundamental and applicative developments**. Intrinsic defects consist in zinc interstitials ( $Zn_i$ ) and oxygen vacancies ( $V_O$ ) acting as donors, zinc vacancies ( $V_{Zn}$ ) and oxygen interstitials ( $O_i$ ) acting as acceptors [4, 5]. For donor defects,  $Zn_i$  is a shallow donor with a low creation energy and justifies that some reports claim that  $Zn_i$  defects account for the n-type behavior.  $V_O$  defects require low formation energy but their deep donor features limit their contribution to n-type conductivity. Thus, the precise structure of the electronic active defects behind the **high conductivity remains an open debate** [5]. For acceptor defects,  $V_{Zn}$  and  $O_i$  are commonly stabilized at higher oxygen partial pressure and accumulate at **grain boundaries**, which **can** hinder the electronic transport and thus decrease electrical conductivity [2]. Hence, it is obvious that the **electrical** performance of n-type ZnO materials is closely related to **the** microstructures.

Various works have been done to regulate the microstructure and thus enhance the performance of n-type ZnO-based materials. Group IIIA elements Al, Ga and In have been used to **substitute** into Zn sites **and** to increase the electrical **conductive** properties **by promoting the excess electrons into the conduction band** at room temperature [6-8]. Dopants like F or Cl **are also expected to play** the same role. Moreover, group IVA elements (Si, Sn) and some transition metal elements (Fe, Ni) were also tried as dopants [9]. **Thereinto, Al-doped ZnO stands out due to the lower cost of Al dopants and higher electrical conductivity ( $\sigma_{RT} = 6.14 \times 10^4$  S/m) compared with other elements leading to n-type doping ZnO** [8]. Besides donor doping, other attempts have been **adopted to increase** the conductivity. The oriented Al-doped ZnO

ceramics exhibited higher electrical conductivity ( $\sigma_{RT} = 1.4 \times 10^5$  S/m) with increasing texture strength [10]. Meanwhile, it is thought that texture ceramics can show modulated microstructures at the grain boundaries, which contribute further increase in conductivity [11]. However, since the complicated design of textured ceramics, the use of thermal treatments is an alternative approach. Neutral and reducing atmosphere have been applied to the sintering process of co-doped ZnO ceramics [12]. In these cases, further incorporation of the dopants (Al and Ti) contributed to increase the charge carriers leading to a drastic increase in conductivity ( $\sigma_{RT} = 2.1 \times 10^5$  S/m). On the other hand, it is expected that the sintering atmosphere with a low oxygen partial pressure limits the formation of acceptor defects at grain boundaries. Therefore, it is also an effective way to enhance the performance of Al-doped ZnO. Nevertheless, it is necessary to point out that potential risks and high cost may restrict its manufacture on a large scale. To date, spark plasma sintering (SPS) shows some advantages like rapid sintering and energy conservation, which has been employed to synthesize various high-performance materials, such as lead-free ferroelectric ceramics  $K_{0.5}Na_{0.5}NbO_3$  (KNN) and transparent ceramics  $MgAl_2O_4$  spinel (MAS) [13, 14]. Furthermore, some previous works have been devoted to ZnO ceramics processed by using SPS. Thus, Ma et al. have obtained high dense and homogeneous Al-doped ZnO ceramics via SPS, where a high electrical conductivity ( $\sigma_{RT} = \sim 7 \times 10^4$  S/m) was involved and led to outstanding thermoelectric performance [15]. Tian et al. reported that co-doped ZnO ceramics obtained via SPS have exhibited a higher electrical conductivity ( $\sigma_{RT} = 2.3 \times 10^5$  S/m) with enormous

concentration of charge carrier ( $2.6 \times 10^{20} \text{ cm}^{-3}$ ) and a metal-like phenomenon of positive temperature coefficient of resistance has been observed [16]. Although it is obvious that SPS method plays a crucial role in preparing ZnO-based ceramics with high electrical conductivity, the microstructure of doped ZnO ceramics after SPS requires deep insights on the related features. Moreover, the electrical conductivity of ZnO ceramics closely correlates with the microstructure of grain and grain boundary, where various intrinsic or extrinsic defects influence greatly the charge transport phenomena. It is necessary to figure out the correlation between the changes in microstructure and the high electrical conductivity. Therefore, the ambition of this work is to contribute by relevant experiments and analyses of such issues.

In this work, Al-doped ZnO ceramics have been prepared by conventional sintering method and SPS method respectively. The microstructure and electrical properties of the samples were compared as function of the sintering method. The results of the electrical measurements of SPS sintered samples display a higher electrical conductivity, up to  $3.0 \times 10^5 \text{ S/m}$  at room temperature. The structure and morphology are systematically investigated and analyzed. Defect effects are discussed from photoluminescence experiments which were analyzed by considering the defect electronic levels involved within ZnO band gap.

## 2. Experiments

### 2.1. Materials

Al-doped ZnO samples with the composition 99.75 mol% ZnO + 0.25 mol%

$\text{Al}_2\text{O}_3$  were prepared by solid state reaction method, and then sintered by the spark plasma sintering (SPS) and the conventional sintering method. The final synthesized ceramic samples were labelled as A-SPS and A respectively. The raw materials, ZnO and  $\text{Al}_2\text{O}_3$ , were firstly ball-milled for 6 h in the deionized water, and then calcined at 450 °C for 3 h after drying. The calcined powders were partly pressed into pellets with 5 wt% polyvinyl alcohol (PVA) solution as the binder under a uniaxial pressure of 200 MPa. After heating at 550 °C for 3 h to release the binder, the prepared pellets were sintered by the conventional sintering method. For conventional sintering method, the pellets were sintered at 1200 °C for 2 h in the air with a heating rate of 5 °C/min and cooled down naturally in the furnace. For SPS method conducted by SPS Syntex society model 515 S, the remainder powders were directly sintered at 1000 °C for 5 min with a heating rate of 100 °C/min under vacuum condition and cooled down to room temperature in 10 min. During the sintering processing, a uniaxial pressure of 65 MPa was applied together with a high pulsed DC current and therefore the samples were protected by boron nitride (BN) and graphite die. After sintering, the dimensions of sample A-SPS are about 15.00 mm as a diameter and 1.50 mm thick, compared to the sample A with 8.67 mm as a diameter and 1.67 mm in thickness.

## 2.2. Characterizations

The structure of both samples was determined by X-ray diffraction (XRD, PANalytical-Empyrean X-ray diffractometer) with Cu-K $\alpha$  radiation source in the 2 $\theta$

range of 30-70°. The morphology of samples was carried out by the scanning electron microscopy (SEM, JEOL JSM 6510LV microscope). The electrical conductive properties were measured by the Quantum Design Physical Property Measurement System (PPMS) in the magnetic field between -1 and 1 T. Before the measurements, a small amount of conductive silver paste was added at four points squarely on one side of the samples to form a good electrical contact and then the four silver dots were connected to the equipment circuit by copper wires. The Raman spectra were recorded by using Raman X-Plora spectrometer equipped by multiple wavelengths (532, 638, 785 nm). In this work, the spectra were recorded in the range 90-1200  $\text{cm}^{-1}$  by using the excitation wavelength  $\lambda = 532$  nm. The UV-vis spectroscopy was studied by the Hitachi U-4100 spectrophotometer with a continuous source ranging from 240 to 2600 nm. The photoluminescence measurements were performed by the LabRAM HR Evolution with the excitation wavelength  $\lambda = 325$  nm.

### **3. Results and discussions**

#### **3.1. Structural and morphological analysis**

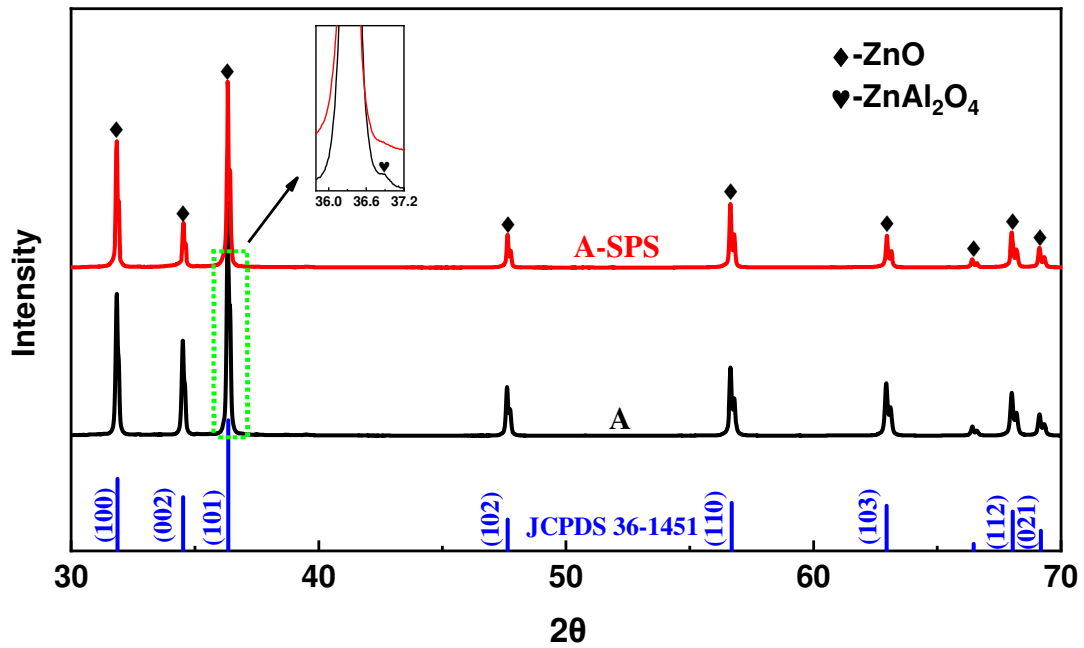


Fig. 1 XRD patterns of the sample A-SPS and sample A with ZnO JCPDS No. 36-1451

The XRD patterns of the sample A-SPS and sample A are shown in Fig. 1. Both diffraction patterns exhibit peaks of the hexagonal wurtzite ZnO (JCPDS No. 36-1451). Noted that only ZnO phase can be observed in sample A-SPS, but the secondary phase of  $\text{ZnAl}_2\text{O}_4$  appears in sample A. This difference between sample A-SPS and A indicates a more efficient incorporation of Al ions in ZnO lattice by using SPS instead to be transformed into a spinel phase for the conventional sintering. The vacuum condition during SPS process may provide an environment with a low oxygen partial pressure, leading to the further substitution of Al into the ZnO lattice. Moreover, due to the high DC current applied in SPS process, a rapid diffusion of Al atoms contributes prudentially to the incorporation of Al ions in the host ZnO lattice instead to form  $\text{ZnAl}_2\text{O}_4$  as a secondary spinel phase.

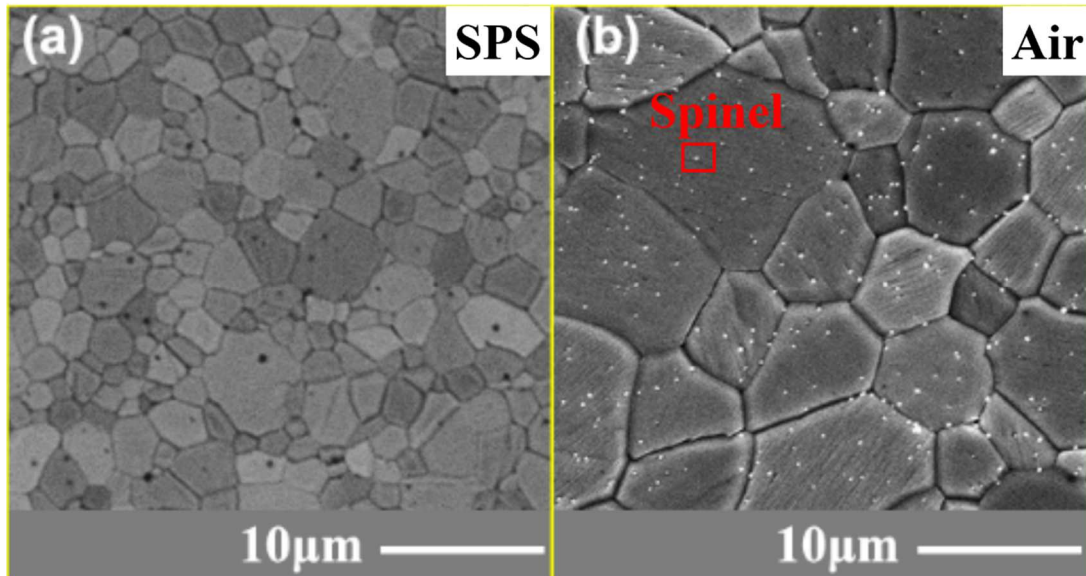


Fig. 2 SEM images of sample A-SPS (a) and sample A (b)

Fig. 2 shows the grain morphologies of the polished and **thermally** etched sample A-SPS and sample A observed by the scanning electron microscope (SEM), where **both samples exhibit the dense structure. Besides, the small black spots in Fig. 2a represent pores while the white spots in Fig. 2b are related to  $ZnAl_2O_4$  grains.** As seen in SEM images, there is great difference in average grain size, with 1.6  $\mu\text{m}$  for sample A-SPS and 8.8  $\mu\text{m}$  for sample A respectively. **The significant decrease of grain size is attributed to the rapid powder densification at the low temperature along with a high pressure.**

### 3.2. Electrical **conductive** properties

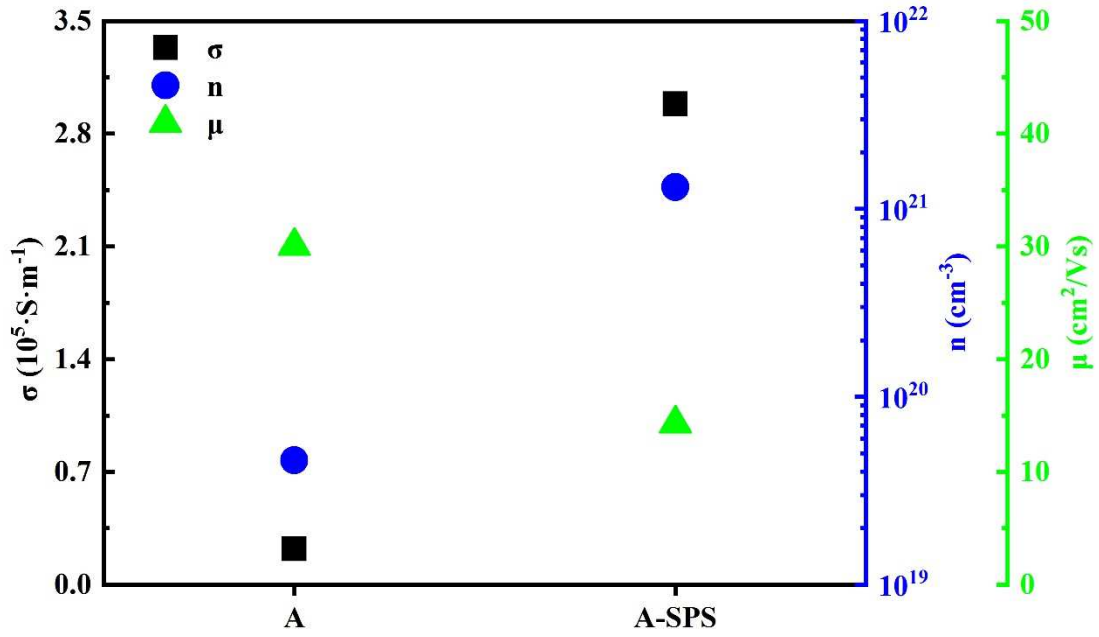


Fig. 3 Electrical **conductive** properties for sample A-SPS and sample A

The electrical conductivities of the sample A-SPS and A, the corresponding carrier concentrations ( $n$ ) and hall mobilities ( $\mu$ ), are depicted in Fig. 3. It is noticed that, **compared to the sample A**, the sample A-SPS exhibits a higher electrical conductivity (for about  $3.0 \times 10^5$  S/m), higher carrier concentration (for about  $1.3 \times 10^{21} \text{ cm}^{-3}$ ), and lower hall mobility (for about  $14.3 \text{ cm}^2 \cdot \text{V}^{-1} \cdot \text{s}^{-1}$ ). The increase of the Al **effective** incorporation concentration in ZnO of sample A-SPS can provide more **charge** carriers, according to Eq. 1:



**Although the contribution of the intrinsic donor defects should be considered when discussing the increase of carrier concentration, its effect is almost negligible when the carrier concentration comes above  $10^{20} \text{ cm}^{-3}$  [17].** Meanwhile, **the lower hall mobility is related to the smaller grain size of sample A-SPS**, since the high quantity of grain boundaries hinder the electronic transport. Therefore, according to **the**

relation ( $\sigma = ne\mu$ ), it can be concluded that higher electrical conductivity of the sample A-SPS originates from the significant increase of carrier concentration.

### 3.3. Raman spectra studies

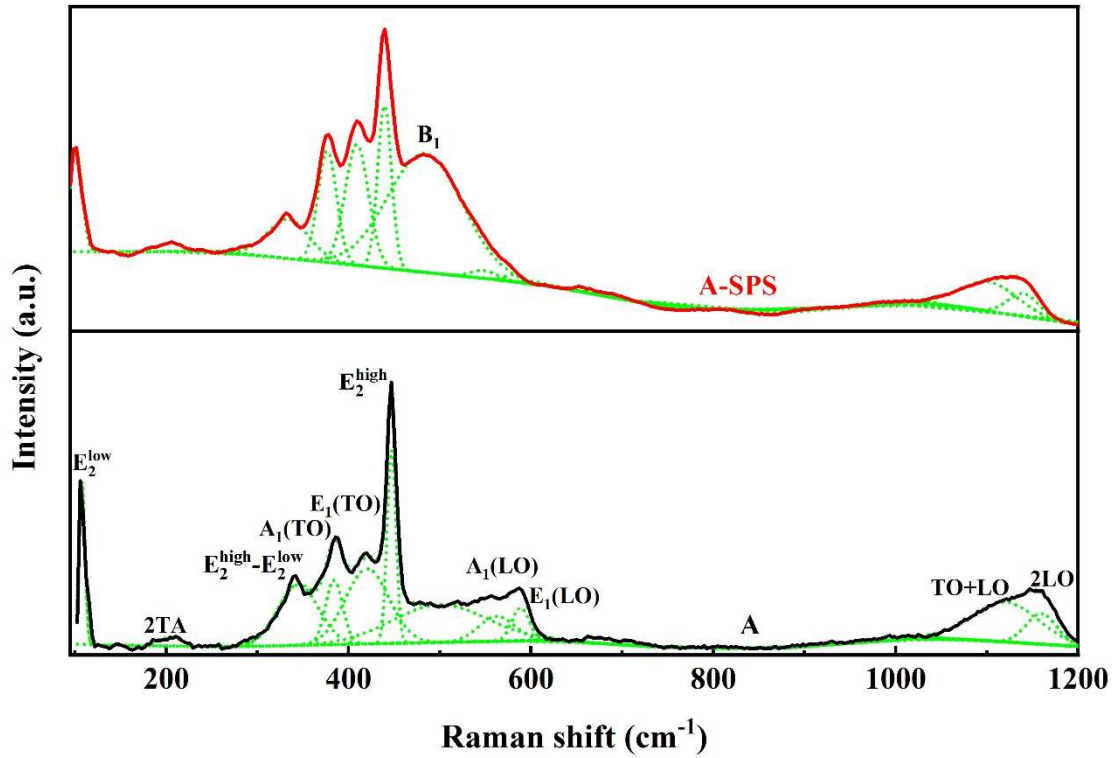


Fig. 4 Raman spectra for sample A-SPS and A

Table 1 Detailed assignments of Raman spectra of sample A-SPS and sample A

| Modes                           | Raman shift (cm <sup>-1</sup> ) |              |          | Changes |
|---------------------------------|---------------------------------|--------------|----------|---------|
|                                 | Reference [18-22]               | Sample A-SPS | Sample A |         |
| <b>First order phonon modes</b> |                                 |              |          |         |
| E <sub>2</sub> <sup>low</sup>   | 100                             | 101          | 106      |         |
| A <sub>1</sub> (TO)             | 380                             | 378          | 385      |         |

|                                |     |     |     |        |
|--------------------------------|-----|-----|-----|--------|
| E <sub>1</sub> (TO)            | 410 | 408 | 419 |        |
| E <sub>2</sub> <sup>high</sup> | 438 | 439 | 447 | Weaken |
| A <sub>1</sub> (LO)            | 584 | 546 | 563 | Weaken |
| E <sub>1</sub> (LO)            | 595 | 579 | 588 | Weaken |

### Second order phonon modes

|   |      |      |      |  |
|---|------|------|------|--|
| 2TA   | 208  | 206  | 204  |  |
| E <sub>2</sub> <sup>high</sup> -E <sub>2</sub> <sup>low</sup> | 336  | 332  | 342  |  |
| TO+LO   | 1090 | 1101 | 1121 |  |
| 2LO   | 1152 | 1138 | 1159 |  |

### Disorder-activated silent mode

|                |   |     |     |            |
|----------------|---|-----|-----|------------|
| B <sub>1</sub> | - | 483 | 500 | Strengthen |
|----------------|---|-----|-----|------------|

To understand the effects of intrinsic and extrinsic defects in ZnO lattice, the vibrational properties probed by Raman are worthy of interest. Following the rules of group theory, there are six active optical phonon modes in the center of the Brillouin zone for the wurtzite lattice structure of ZnO, which are summarized as  $\Gamma_{\text{opt}} = A_1 + 2B_1 + E_1 + 2E_2$  [18]. Among them, B<sub>1</sub> mode is not a Raman active mode in the perfect ZnO bulk crystalline structure and silent in the spectra. Both A<sub>1</sub> and E<sub>1</sub> modes are active polar modes and therefore they are refined to distinguish between two geometry arrangements: transverse optical (TO) and longitudinal optical (LO) phonon modes. The E<sub>2</sub> mode is a non-polar mode and consists in two different frequency phonon modes, E<sub>2</sub><sup>low</sup> and E<sub>2</sub><sup>high</sup>, respectively. Fig. 4 displays the Raman spectra in the range 90-1200 cm<sup>-1</sup> for both sample A-SPS and A measured at room temperature. As

observed in Reference [18-22], active modes corresponding to wurtzite ZnO mentioned above have been detected and assigned:  $E_2^{\text{low}}$  at  $100\text{ cm}^{-1}$ ,  $E_2^{\text{high}}$  at  $438\text{ cm}^{-1}$ ,  $A_1(\text{TO})$  at  $380\text{ cm}^{-1}$ ,  $E_1(\text{TO})$  at  $410\text{ cm}^{-1}$ ,  $A_1(\text{LO})$  at  $584\text{ cm}^{-1}$  and  $E_1(\text{LO})$  at  $595\text{ cm}^{-1}$ . Additionally, some second order phonon modes are also resolved in the spectra, such as  $2\text{TA}$  at  $208\text{ cm}^{-1}$ ,  $E_2^{\text{high}} - E_2^{\text{low}}$  at  $336\text{ cm}^{-1}$ ,  $\text{TO} + \text{LO}$  at  $1090\text{ cm}^{-1}$ , and  $2\text{LO}$  at  $1152\text{ cm}^{-1}$ . Both samples show the similar results with the former reported work. Moreover, an anomalously broad peak can be observed at about  $500\text{ cm}^{-1}$  in both samples and this peak appears in the symmetric forbidden scattering configuration of wurtzite ZnO. According to some previous work, this peak is related to the disorder-activated  $B_1$  mode and its presence can exhibit more specifics about incorporation of Al elements and structural disorder in ZnO host lattice [18, 19].

In comparison of sample A, sample A-SPS shows some significant changes in Raman spectra. The  $E_2^{\text{high}}$  peak, which is sensitive to crystal quality, exhibits a lower intensity. The Al substitution into Zn site can form the structural defects and local lattice distortion, which causes the decrease of the intensity of  $E_2^{\text{high}}$  mode in sample A-SPS [22]. The Al ions substitute randomly into the Zn sublattice, which also breaks the translational symmetry. In a perfect crystalline structure, only phonons at the center of Brillouin zone can be observed in Raman spectra. However, the break of the translational symmetry causes that the phonons around the center of Brillouin zone can also be detected [20]. Hence, the  $B_1$  Raman peak is silent in perfect crystalline structure but can be activated in a disordered structure. Thus, sample A-SPS shows an obvious increase in  $B_1$  mode intensity and further implies the structural distortion

becomes more significant. These two peaks together prove the weakened lattice periodicity due to the Al substitution into Zn sites. Moreover, the  $A_1(\text{LO})$  and  $E_1(\text{LO})$  peaks almost disappear in sample A-SPS. The same phenomena were reported in Al-doped ZnO powders annealed in hydrogen and attributed to the excess Zn [23]. Other former works also considered these two LO modes closely relate to nonstoichiometric Zn/O ratio, like forming oxygen vacancy ( $V_{\text{O}}$ ) or zinc interstitial ( $\text{Zn}_i$ ) [22]. That means the larger amount of intrinsic donor defects contribute to lattice disorder which suppress these two modes. Detailed assignments of the Raman mode are summarized in Table 1 with reference to their evolution with the sintering method. These features can finally manifest that, under the SPS condition, further incorporation of Al elements and further formation of intrinsic donor defects result aggravation of structural distortion.

#### **3.4. Absorption and luminescence studies**

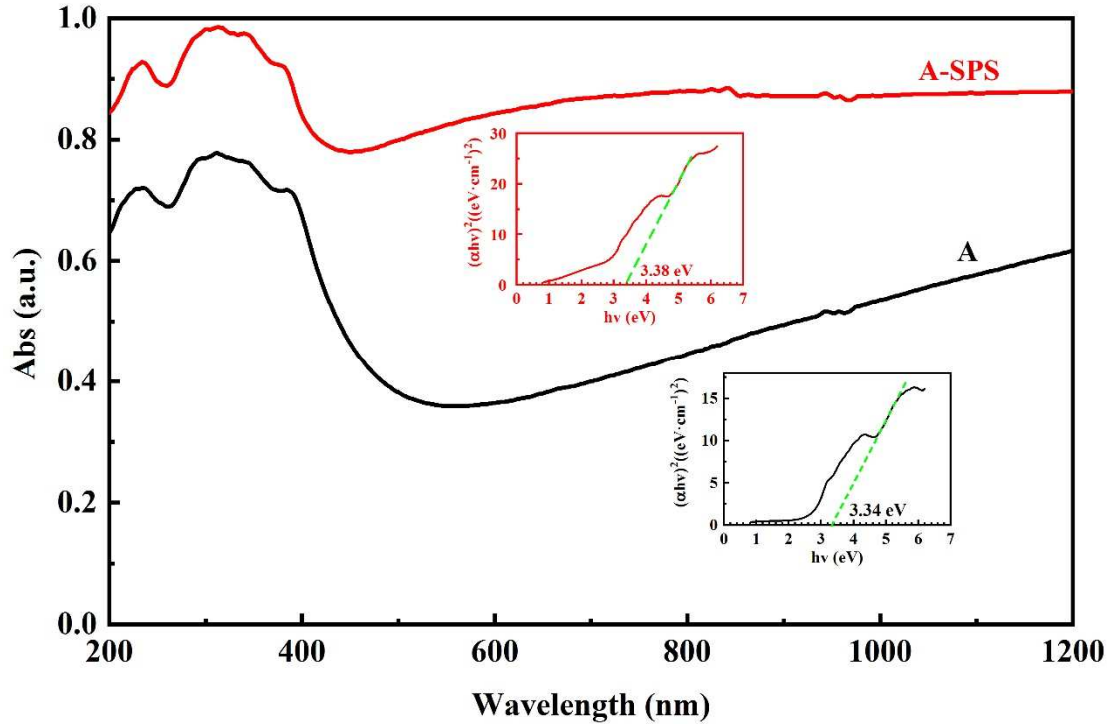


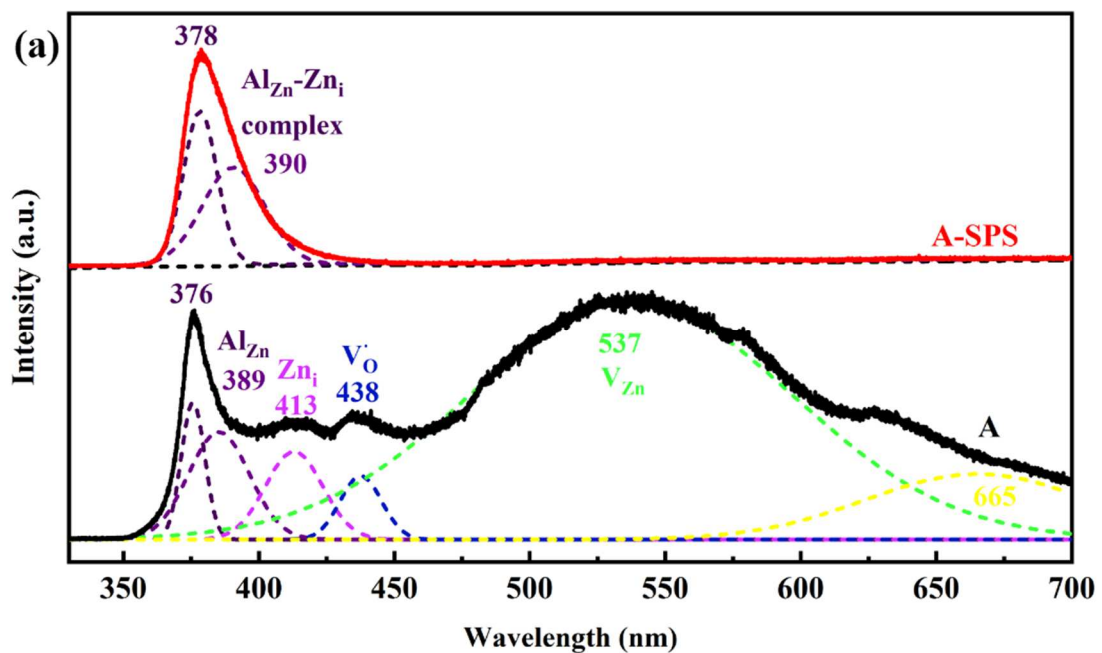
Fig. 5 UV-vis absorption spectra for sample A-SPS and A and the inset shows Tauc plots  $(\alpha hv)^2$  versus  $hv$

There is no doubt that optical absorption and emission can reflect the electronic structure of the underlying lattice as well as that of electronic defects levels and the recombination processes. The comparative optical absorption spectra of sample A-SPS and A depicted in Fig. 5 inform the above features. The optical absorption curves for the two samples shown in the wavelength from 200 to 1200 nm underline some differences in the spectra shape and the Tauc plots in the inset. There are sharp decreases in the absorbance at shoulder peak near 385 nm, which is related to the optical band gap. Compared with sample A, the absorption edge of sample A-SPS exhibits a slight blue shift, indicating the broadening of optical band gap. More details can be displayed by the relation between the absorption coefficient  $\alpha$  and the photon energy  $hv$  by using the function in Eq. 2 [24].

$$\alpha hv = B(hv - E_g)^n \quad (2)$$

Here, **B is an energy independent constant**,  $E_g$  is the band gap and  $n$  depends on the type of transition. Thereinto,  $n = 0.5$  for permissive direct transition type semiconductor, 1.5 for forbidden direct transition type semiconductor, 2 for permissive indirect transition type semiconductor and 3 for forbidden indirect transition type semiconductor, respectively. Due to permissive direct band transition type for wurtzite ZnO,  $n = 0.5$  and Tauc plots  $(\alpha hv)^2$  versus  $hv$  are shown in the inset of Fig. 5. From the intersection between the asymptote of the Tauc plot and the energy ( $hv$ ), the optical band gap is found to be 3.38 eV and 3.34 eV, for sample A-SPS and A respectively. The blue shift and the increase of optical band gap is attributed to the Burstein-Moss effect [25], which implies that there are more free electrons occupying at the bottom of the conduction band in sample A-SPS than that in sample A. The further incorporation of Al ions is responsible for this result. **Furthermore, the strong absorption in the visible and near IR region of the spectra with a higher intensity in the A-SPS sample compared to that in the sample A. These absorption features are related to free electron absorption in occupied states induced by Al impurities and illustrate that there is a higher quantity of electrons on the conduction band of sample A-SPS than sample A [25]. On the other hand, the concentration of the free carriers induces the phenomena of a plasma resonance which is characterized by an optical absorption curve at a wavelength  $\lambda_p \sim \sqrt{\frac{m^*}{n}}$ , where  $m^*$  represents the effective mass of the charge carrier and  $n$  the concentration of free carriers [26]. Thus, the broad feature which extends on the visible and near IR region range traduces the plasma resonance**

phenomena in sample A-SPS and A. Further incorporation of Al elements in sample A-SPS leads to a higher carrier concentration which is traduced in the absorption spectra in agreement with electrical conduction results. Coming now to the shoulders observed on the absorption spectra in the high energy side and illustrated by two main bands centered between 3 and 4 eV and extending down to 2 eV as clearly illustrated from Tauc plot. The origin of these details on the absorption spectra is intimately related to the electronic active defects which coexist in ZnO structure. As discussed in the section on Raman studies, the defects are intrinsic such as oxygen or Zn vacancies, interstitial Zn,.. or extrinsic defects caused by Al doping. The precise nature of the defects and their related electronic levels with ZnO band gap can be clarified from Photoluminescence (PL) experiments which are discussed below.



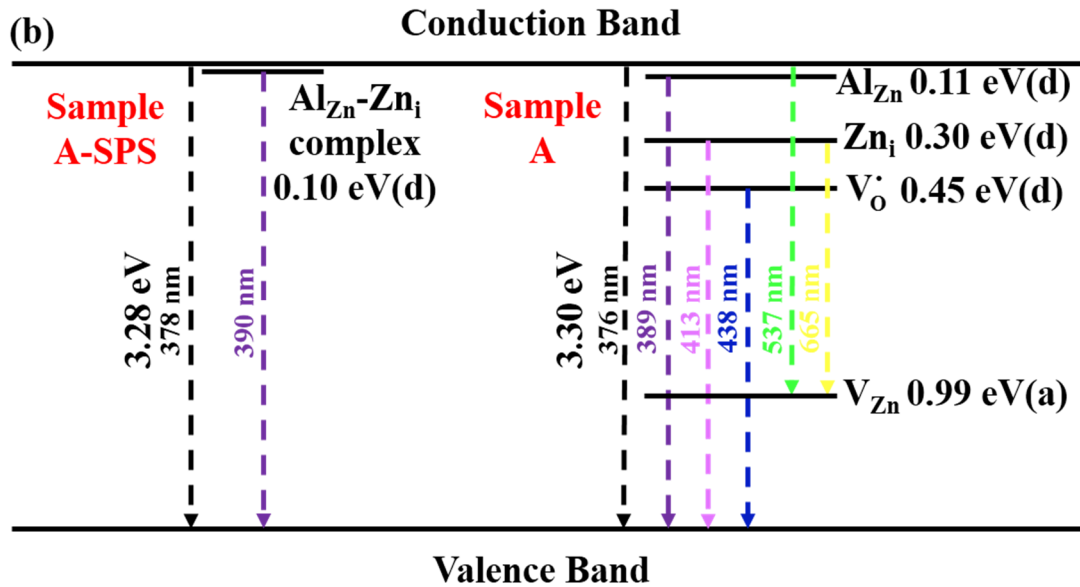


Fig. 6 (a) Photoluminescence spectra for sample A-SPS and sample A, and (b) the corresponding diagram of the luminescence emission for sample A-SPS and sample A

Photoluminescence (PL) spectroscopy for both sample A-SPS and A have been measured at room temperature with the excitation of 325 nm and the spectra are presented in Fig. 6a. For both samples, PL spectra consist in two emission band with the one is related to UV emission and the other one is related to deep level emission. The UV emission band located at around 375 nm, originates from the transition of excitons and namely near band edge (NBE) emission. In the visible region, deep level emission is attributed to the intrinsic structural defects, like zinc interstitials ( $\text{Zn}_i$ ) or oxygen vacancies ( $\text{V}_O$ ) as donor defects and zinc vacancies ( $\text{V}_{\text{Zn}}$ ) or oxygen interstitials ( $\text{O}_i$ ) as acceptor defects. These defects can become luminescence centers after suitable excitation. As shown for sample A, the band at 389 nm is due to the shallow donor  $\text{Al}_{\text{Zn}}$  level according to DFT calculation [9]. the violet emission located at 413 nm is considered to be related to electron transition from  $\text{Zn}_i$  level to the top of

valence band (VB) [27]. Then, the transition from single ionized  $V_O$  level to the top of VB is responsible for the blue emission at 435 nm [28]. A broad green emission is found at 535 nm, which is generally attributed to the transition from the bottom of conduction band (CB) to some deep acceptor level like  $V_{Zn}$  and  $O_i$  [29, 30]. Due to high formation energy of  $O_i$ , it is more likely that  $V_{Zn}$  acts as the luminescence center [4]. At 665 nm, the yellow emission band is assigned the transition from the donor  $Zn_i$  level to the deep acceptor level  $V_{Zn}$ . No luminescence band corresponding to the  $ZnAl_2O_4$  phase is found in both spectra probably due to its low concentration in the sample A. However, for the sample A-SPS, the PL spectrum becomes simple, where an asymmetrical emission band only leaves. To some extent, the intensity of emission bands correspond to the concentrations of defects. Therefore, the vanish of green and yellow emission bands implies excessively low concentrations of the intrinsic acceptor defects. Although the decreased concentrations of the intrinsic acceptor defects may increase the hall mobility, the increased quantity of grain boundary enhances the electron scattering and limits the impact from intrinsic acceptor defects [12]. Moreover, for the asymmetrical emission band in sample A-SPS, it is thought to be the combination of two emission bands. One component is related to NBE emission, the other one is from the shallow donor level very closed to the conduction band and related to Al impurities as mentioned above. It is worth noting also, that the PL bands assigned to  $Zn_i$  and  $V_O$  have been almost disappeared in contradiction with the results that intrinsic donor defects suppress the  $A_1(LO)$  and  $E_1(LO)$  modes in Raman spectra. Therefore, these donor defects may combine with Al-doped defects to

form defect complexes leading also to the shallow donor level. Momot et al. exhibited the evidences of existence of  $\text{Al}_{\text{Zn}}\text{-Zn}_i$  complexes after first-principle calculation and NMR measurement [31]. The authors concluded that Al substitution in a tetrahedral Zn site ( $\text{Al}_{\text{Zn}}$ ) combined with an interstitial Zn ( $\text{Zn}_i$ ) is characterized by low defect energy formation. Sun et al. also discussed some similar results in co-doped ZnO ceramics with the high conductive properties accounted for  $\text{Al}_{\text{Zn}}\text{-Zn}_i$  complexes by EPR and NMR results [32]. Hence, it is rational to consider that  $\text{Al}_{\text{Zn}}\text{-Zn}_i$  complexes may account for violet emission in the PL spectra. The corresponding diagrams of the luminescence emission for sample A-SPS and A are shown in Fig. 6b. From this diagram, it is clear that the  $\text{Al}_{\text{Zn}}\text{-Zn}_i$  complexes act as the only donor to provide electrons to the conduction band and its energy level is slightly closer to the conduction band than  $\text{Al}_{\text{Zn}}$  level, which implies that it can associate with the obtained huge electrical conductivity. Thus and as a matter of fact, the features of PL spectra in sample A-SPS and A, support that,  $\text{Al}_{\text{Zn}}\text{-Zn}_i$  complexes appear with the increased Al doping concentration by using SPS method which contribute efficiently to enhance the electrical conductive properties.

#### 4. Conclusion

Al-doped ZnO with high electrical conductivities up to  $3.0 \times 10^5$  S/m have been obtained in samples prepared by the SPS sintering method. SEM experiments show different microstructures between the SPS method (sample A-SPS) and the

conventional sintering method (sample A). The structural features inferred from XRD studies are marked by a secondary phase  $\text{ZnAl}_2\text{O}_4$  in sample A while an increase is suggested for the solubility limit of Al in ZnO lattice. The variation of Raman spectra point out the relevance of structural distortions with the incorporation of Al ions in the host ZnO lattice and the increased concentration of intrinsic defects such as interstitial Zn and oxygen vacancies. The UV-Vis absorption spectra show a slight increase of the optical band gap, the involvement of electronic active defects within the gap and the large carrier concentrations leading to plasma resonance effects. The PL spectra bring consistent insights on the  $\text{Al}_{\text{Zn}}\text{-Zn}_i$  defect complexes as well as the absence of acceptor defects. With their shallow levels and the favored formation of  $\text{Al}_{\text{Zn}}\text{-Zn}_i$  defect complexes in sample A-SPS, these defects correlate with the highly achieved electrical conductivity in Al doped ZnO ceramics.

## **Acknowledgments**

Projects supported by the National Key R&D Program of China (No. 2016YFA0201103, 2016YFB0402701), the National Basic Research Program of China under Grant (No. 2015CB654605), National Nature Science Foundation of China (No. 51831010, 51672293, 51807195) and the Instrument Developing Project of Chinese Academy of Sciences (No. ZDKYYQ20180004). Q. Sun would like to thank Campus France for the Excellence Eiffel Grant (2017–2018) at Le Mans University.

## References

- [1] U. Ozgur, Y.I. Alivov, C. Liu, A. Teke, M.A. Reshchikov, S. Dogan, V. Avrutin, S.J. Cho, H. Morkoc, A comprehensive review of ZnO materials and devices, *J Appl Phys*, 98 (2005).
- [2] T.K. Gupta, Application of Zinc-Oxide Varistors, *J Am Ceram Soc*, 73 (1990) 1817-1840.
- [3] P. Keil, M. Trapp, N. Novak, T. Fromling, H.J. Kleebe, J. Rodel, Piezotronic Tuning of Potential Barriers in ZnO Bicrystals, *Advanced Materials*, 30 (2018).
- [4] A. Janotti, C.G. Van de Walle, Native point defects in ZnO, *Phys Rev B*, 76 (2007).
- [5] M.D. McCluskey, S.J. Jokela, Defects in ZnO, *J Appl Phys*, 106 (2009).
- [6] L. Han, L.T. Hung, N. van Nong, N. Pryds, S. Linderoth, The Influence of Spark Plasma Sintering Temperature on the Microstructure and Thermoelectric Properties of Al,Ga Dual-Doped ZnO, *J Electron Mater*, 42 (2012) 1573-1581.
- [7] S. Farid, S. Mukherjee, K. Sarkar, M. Mazouchi, M.A. Stroschio, M. Dutta, Enhanced optical properties due to indium incorporation in zinc oxide nanowires, *Appl Phys Lett*, 108 (2016).
- [8] M. Ohtaki, T. Tsubota, K. Eguchi, H. Arai, High - temperature thermoelectric properties of  $(\text{Zn}_{1-x}\text{Al}_x)\text{O}$ , *J Appl Phys*, 79 (1996) 1816-1818.
- [9] K. Ellmer, A. Bikowski, Intrinsic and extrinsic doping of ZnO and ZnO alloys,

Journal of Physics D: Applied Physics, 49 (2016).

[10] H. Kaga, Y. Kinemuchi, H. Yihnaz, K. Watarl, H. Nakano, H. Nakano, S. Tanaka, A. Makiya, Z. Kato, K. Uernatsu, Orientation dependence of transport property and microstructural characterization of Al-doped ZnO ceramics, *Acta Mater*, 55 (2007) 4753-4757.

[11] J.L. Ning, D.M. Jiang, K.H. Kim, K.B. Shim, Influence of texture on electrical properties of ZnO ceramics prepared by extrusion and spark plasma sintering, *Ceramics International*, 33 (2007) 107-114.

[12] T. Tian, L.H. Cheng, L.Y. Zheng, J.J. Xing, H. Gu, S. Bernik, H.R. Zeng, W. Ruan, K.Y. Zhao, G.R. Li, Defect engineering for a markedly increased electrical conductivity and power factor in doped ZnO ceramic, *Acta Mater*, 119 (2016) 136-144.

[13] M. Bah, F. Giovannelli, F. Schoenstein, G. Feuillard, E. Le Clezio, I. Monot-Laffez, High electromechanical performance with spark plasma sintering of undoped  $K_{0.5}Na_{0.5}NbO_3$  ceramics, *Ceramics International*, 40 (2014) 7473-7480.

[14] A. Pille, H. Spiridigliozzi, M. Amamra, T. Billeton, M. Zaghrioui, E. Feldbach, A. Kanaev, F. Schoenstein, Morphology and luminescence of  $MgAl_2O_4$  ceramics obtained via spark plasma sintering, *Ceramics International*, 45 (2019) 8305-8312.

[15] N. Ma, J.F. Li, B.P. Zhang, Y.H. Lin, L.R. Ren, G.F. Chen, Microstructure and thermoelectric properties of  $Zn_{1-x}Al_xO$  ceramics fabricated by spark plasma sintering, *J Phys Chem Solids*, 71 (2010) 1344-1349.

[16] T. Tian, L.H. Cheng, J.J. Xing, L.Y. Zheng, Z.Y. Man, D.L. Hu, S. Bernik, J.T.

- Zeng, J. Yang, Y. Liu, G.R. Li, Effects of sintering on the microstructure and electrical properties of ZnO-based thermoelectric materials, *Mater Design*, 132 (2017) 479-485.
- [17] Y. Natsume, H. Sakata, Electrical conductivity and optical properties of ZnO films annealed in hydrogen atmosphere after chemical vapor deposition, *Journal of Materials Science-Materials in Electronics*, 12 (2001) 87-92.
- [18] J. Serrano, A.H. Romero, F.J. Manjón, R. Lauck, M. Cardona, A. Rubio, Pressure dependence of the lattice dynamics of ZnO: An ab initio approach, *Phys Rev B*, 69 (2004).
- [19] F.J. Manjón, B. Marí, J. Serrano, A.H. Romero, Silent Raman modes in zinc oxide and related nitrides, *J Appl Phys*, 97 (2005).
- [20] H.K. Yadav, K. Sreenivas, R.S. Katiyar, V. Gupta, Defect induced activation of Raman silent modes in rf co-sputtered Mn doped ZnO thin films, *Journal of Physics D: Applied Physics*, 40 (2007) 6005-6009.
- [21] C. Li, J. Lv, Z. Liang, S. Yao, Study on the optical absorption and green emission of ZnO phosphors by varying Al doping contents, *Opt Mater*, 35 (2013) 586-589.
- [22] S. Das, S. Das, S. Sutradhar, Effect of Gd<sup>3+</sup> and Al<sup>3+</sup> on optical and dielectric properties of ZnO nanoparticle prepared by two-step hydrothermal method, *Ceramics International*, 43 (2017) 6932-6941.
- [23] C. Li, J. Lv, B. Zhou, Z. Liang, Influence of annealing atmosphere on optical properties of Al-doped ZnO powders, *physica status solidi (a)*, 209 (2012) 1538-1542.
- [24] N.R. Yogamalar, A. Chandra Bose, Absorption–emission study of hydrothermally grown Al:ZnO nanostructures, *Journal of Alloys and Compounds*, 509 (2011)

8493-8500.

[25] A. Slassi, S. Naji, A. Benyoussef, M. Hamedoun, A. El Kenz, On the transparent conducting oxide Al doped ZnO: First Principles and Boltzmann equations study, *Journal of Alloys and Compounds*, 605 (2014) 118-123.

[26] D. Das, L. Karmakar, Optimization of Si doping in ZnO thin films and fabrication of n-ZnO:Si/p-Si heterojunction solar cells, *Journal of Alloys and Compounds*, 824 (2020).

[27] L. Xu, G. Zheng, H. Wu, J. Wang, F. Gu, J. Su, F. Xian, Z. Liu, Strong ultraviolet and violet emissions from ZnO/TiO<sub>2</sub> multilayer thin films, *Opt Mater*, 35 (2013) 1582-1586.

[28] X.Y. Ma, Z. Wang, J.W. Song, J.H. Yao, Optical properties of ZnO and Mn-doped ZnO nanocrystals fabrication by vapor phase transport processes, *Nano-Micro Letters*, 1 (2010).

[29] Y. Gong, T. Andelman, G.F. Neumark, S. O'Brien, I.L. Kuskovsky, Origin of defect-related green emission from ZnO nanoparticles: effect of surface modification, *Nanoscale Res Lett*, 2 (2007) 297-302.

[30] H. Zeng, G. Duan, Y. Li, S. Yang, X. Xu, W. Cai, Blue Luminescence of ZnO Nanoparticles Based on Non-Equilibrium Processes: Defect Origins and Emission Controls, *Advanced Functional Materials*, 20 (2010) 561-572.

[31] A. Momot, M.N. Amini, G. Reekmans, D. Lamoen, B. Partoens, D.R. Slocombe, K. Elen, P. Adriaensens, A. Hardy, M.K. Van Bael, A novel explanation for the increased conductivity in annealed Al-doped ZnO: an insight into migration of

aluminum and displacement of zinc, *Phys Chem Chem Phys*, 19 (2017) 27866-27877.

[32] Q. Sun, T. Tian, L. Zheng, Z. Man, G. Li, M. Barré, J. Dittmer, A. Bulou, A.H. Kassiba, Electronic active defects and local order in doped ZnO ceramics inferred from EPR and  $^{27}\text{Al}$  NMR investigations, *Journal of the European Ceramic Society*, 39 (2019) 3070-3076.